$H'_{Re}(t_{max}, f_0)$ and $H'_{Im}(t_{max}, f_0)$ are the real and imaginary parts of $H'(t_{max}, f_0)$ with lag time, L. t_{max} is the time when the dynamic gain is maximum.

Static Characteristics

After the RSNA, AP, and HR during the last 10 s of each CSP level were averaged using the data of the step-input protocol, the static characteristics of total baroreflex loop, neural arc, and cardiac baroreflex control were examined by regression analysis for the logistic function.[24,46,47] To quantify static characteristics of the peripheral arc, linear regression analysis was performed. The closed-loop operating point of the baroreflex (AP_{OP}) was determined from the intersection point between the CSP-AP curve (total baroreflex loop) and CSP-AP identity line. AP_{OP} was also determined from AP at the intersection point between the CSP-RSNA curve (neural arc) and RSNA-AP line (peripheral arc) in the equilibrium diagram.[18]

Standard Analysis

The STFFT as a traditional time-frequency method was applied to the step-input (±20 mmHg) protocol, using the model response between CSP and AP (see Appendix). The time window was set to 12.8 s (64 data points) and 51.2 s (256 points, which is close to that at the lowest frequency in the used wavelet method). After the application of the detrend and Hanning window, power spectral densities of the CSP and AP and the transfer gain of the cross-spectra were computed every 200 ms. In the STFFT (256 points), pseudo-random noises were added to the input (within ±0.1 mmHg) and output (±1 mmHg every 200 ms) signals. The STFFT analysis was also compared with the proposed wavelet analysis over frequencies under the pseudo-random noise within ±0.1 mmHg in the input and ±1 or ±2 mmHg in output every 200 ms.

Experiment of Bezold-Jarisch Reflex

To elucidate the modified wavelet-based analysis in the pathophysiological condition, the previous datasets assessing static baroreflex during BJR[18] were reanalyzed; the data at sampling rate of 200 Hz were averaged every 40 points. In 8 anesthetized rabbits with sectioned aortic depressor nerves, intact vagi, and isolated carotid sinuses, CSP was increased stepwise while AP and HR were recorded before and after 7-min administration of a serotonin ($5\text{-}HT_3$) receptor agonist, phenylbiguanide (PBG, 100 μg/kg/min, intravenous infusion): Control and PBG conditions. Vagal afferent was confirmed as the main pathway of the BJR induced by intravenous PBG infusion.[20]

Cardiac Baroreflex

The role of cardiac baroreflex (CSP to HR response) was studied, focusing on the contribution of the cardiac sympathovagal activity to dynamic baroreflex for AP regulation. The ratio of the transfer functions between cardiac baroreflex and total (CSP-AP) loop was calculated under Control and PBG conditions, using the results from the proposed analysis.

Statistical Analysis

All data are expressed as mean ± SEM. The gain, power, and frequency in the figures are shown in log scales. The transfer functions in the neural and peripheral arcs were normalized in each animal so that the average gain in all stepwise changes of normal condition became unity at 0.04 Hz. To test the difference among six stepwise changes or between the Control and PBG conditions, we obtained the gain at 0.04 ($G_{0.04}$), the average slope of the gains between 0.1 to 0.4 Hz (Slope), and the lag time in each animal. One-way analysis of variance with multiple comparisons using Bonferroni correction[9] was applied to assess the level differences. Differences were considered statistically significant at $p < 0.05$.

Simulation for Closed-Loop Baroreflex

The carotid sinus open-loop animal experiment should be linked to human closed-loop baroreflex to explore the possibility of applying the proposed analysis to clinical diagnosis. We performed a simulation study, using the emulated cardiac baroreflex model from observed AP input to observed HR output under the closed-loop AP response (see Appendix) to test the accuracy of the proposed wavelet-based analysis and to acquire the transfer functions of the cardiac baroreflex for use in human laboratory test.

RESULTS

Test of Wavelet Analysis

The proposed wavelet-based analysis was tested using the baroreflex model response between CSP and AP under carotid sinus open-loop condition (see Appendix). After the calculation of the wavelet power spectrum for the input and the input-output cross spectrum (Fig. 2a), the transfer function was acquired (Fig. 2b). The gains reached the maximum immediately after the step input at 60 s and the phase changed greatly when approaching the maximum gain. Bode plots were extracted from the maximum points of the time-course transfer function with and without

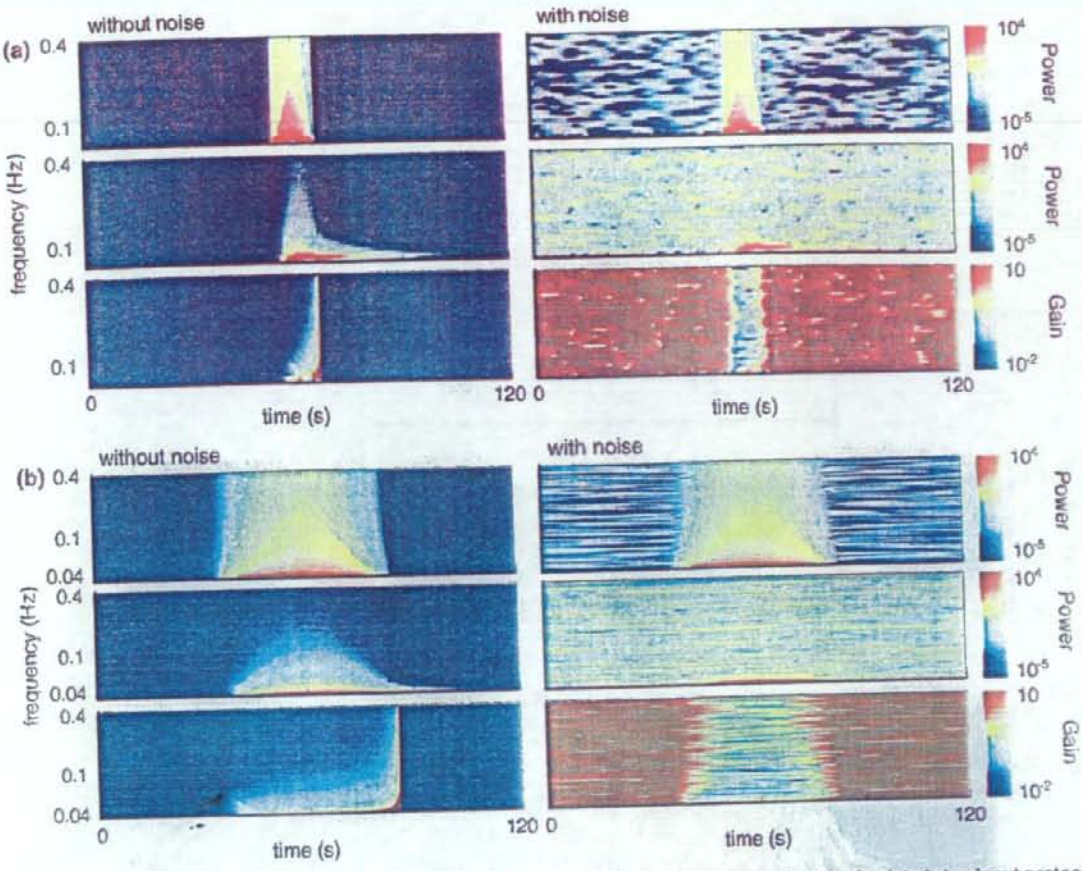

FIGURE 1. Time-frequency method based on the short-time FFT for system identification using the simulated step-input protocol. Time windows, 12.8 s (a) and 51.2 s (b). Power spectral densities of carotid sinus pressure (CSP) input (*top*) and arterial pressure (AP) output (*middle*) and transfer gain (*bottom*) in the absence (*left*) or presence (*right*) of pseudo-random noises.

background noise (Fig. 2c). In the presence of pseudo-random noise (within ±0.01 mmHg in input and ±1 mmHg in output changed every 200 ms), the transfer function closely resembled the theoretical values. Compared to the STFFT (Fig. 1), the proposed wavelet method could accurately estimate the transfer function over different frequencies, regardless of a poor signal to noise (S/N) ratio at higher frequency, because of the property of the step input power (Fig. 2d).

Dynamic Baroreflex

The averaged RSNA, AP, and HR responses to the step-input changes were decreased with the increments in CSP from 40 to 160 mmHg every minute ($n = 8$, Fig. 3a). In the averaged time series ($n = 8$, Fig. 3b), the power spectrums at all step inputs were the same values at each frequency level because of a constant change of +20 mmHg (greater in low frequency and smaller in high frequency). The powers of RSNA, AP, and HR change were higher at CSP_{80-100} than other CSP changes over all frequency ranges, and the magnitudes were especially small at low or high CSP changes.

The averaged ($n = 8$) time series of transfer functions in the neural arc (a), peripheral arc (b), total loop (c) and cardiac baroreflex (d) were calculated after wavelet transform (Fig. 4). In the neural arc, gain values in low frequencies were much less at CSP changes away from the operating point. In the peripheral arc, low pass characteristics in the gains were observed at all CSP changes except the lowest CSP_{40-60} change reflecting spontaneous neural firing. In the total baroreflex loop, the gains at CSP changes within 60–120 mmHg were higher than those at other CSP changes, indicating low-pass characteristics. In the cardiac baroreflex, the gains were smaller at the

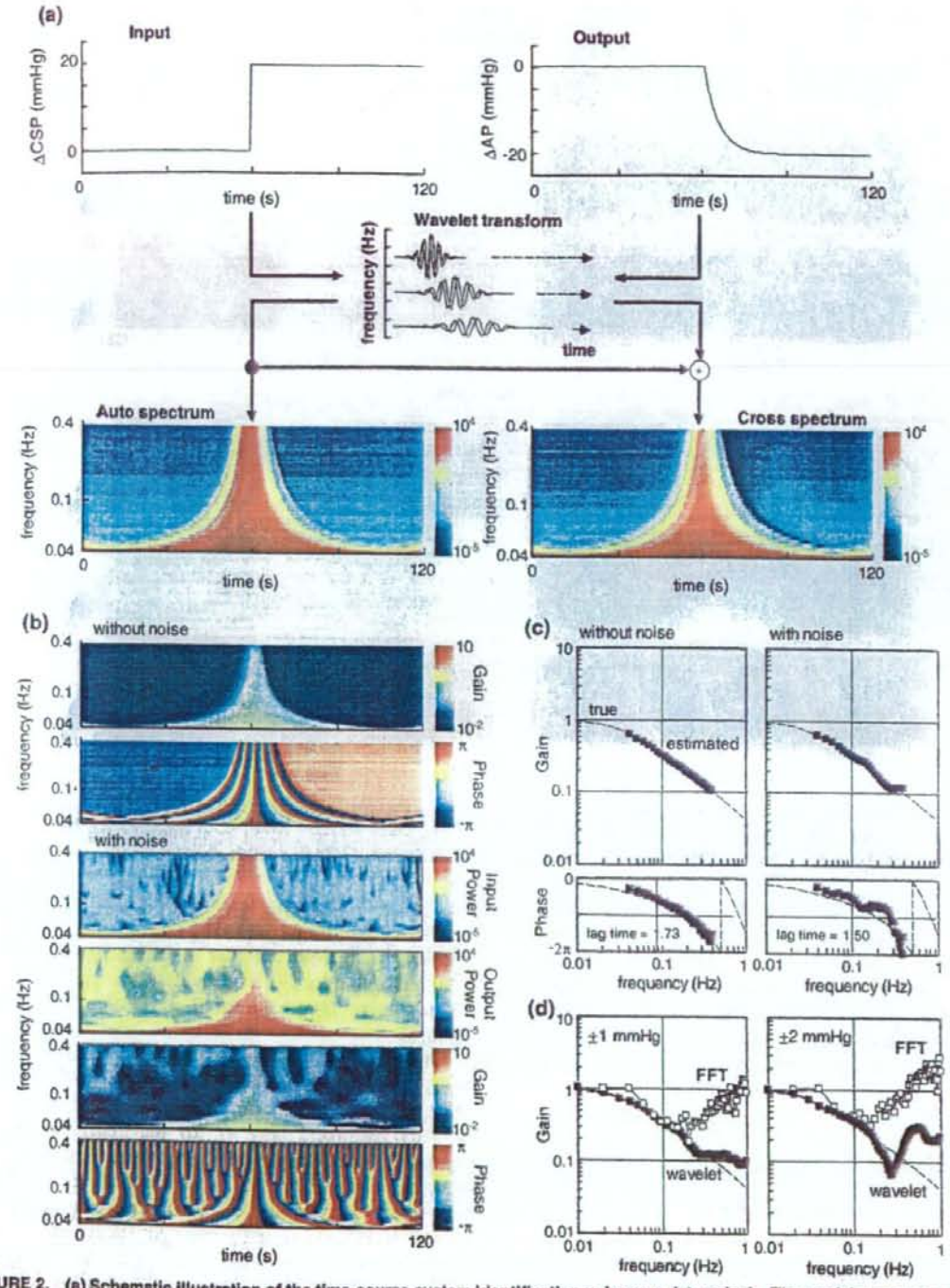

FIGURE 2. (a) Schematic illustration of the time-course system identification using wavelet analysis. The model response of total loop from CSP to AP under the carotid sinus open-loop condition was assessed for 120 s. Step input change of 20 mmHg was added to the system at 60 s. The time-series transfer function estimated by our wavelet analysis (b) and transfer function extracted from the time-course data of the total loop transfer function and the theoretical data (c). Gain (*top*) and phase (*bottom*) in the absence or presence of pseudo-random noise. (d) Gains in the short-time FFT and proposed wavelet analyses over wide frequencies (0.01–1 Hz) under the pseudo-random noise [±1 mmHg (*left*) and ±2 mmHg (*right*)].

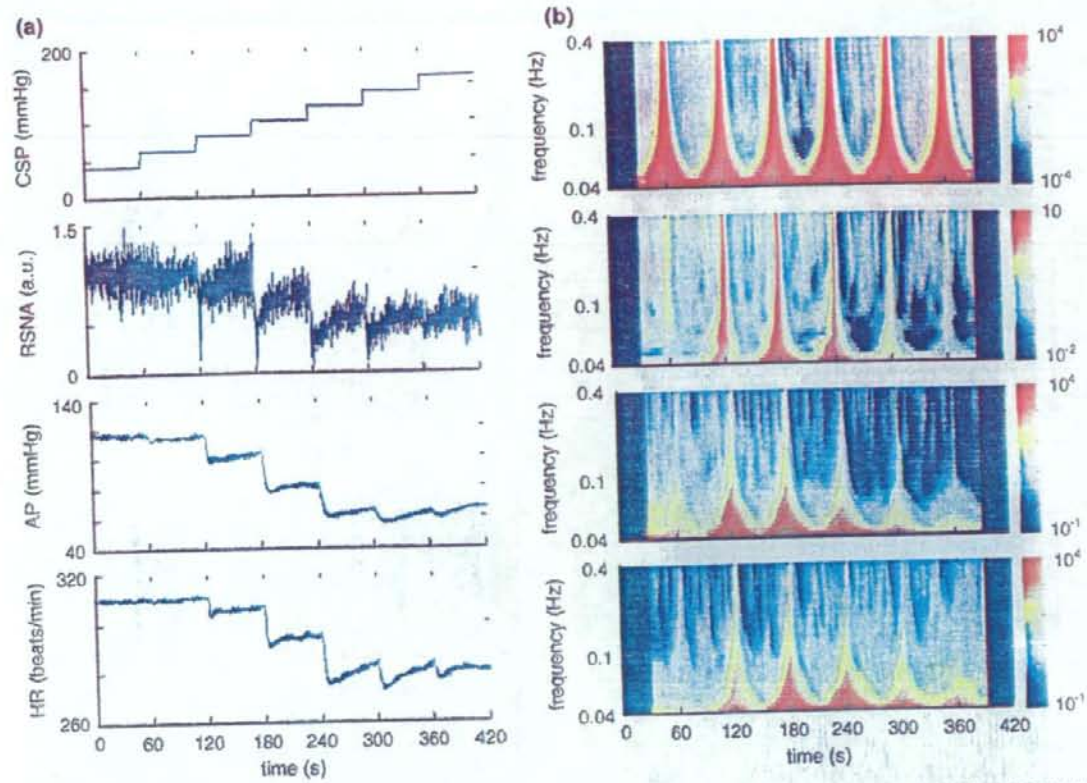

FIGURE 3. Averaged time series (a, $n = 8$) and wavelet power (b, $n = 8$) of CSP, renal sympathetic nerve activities (RSNA), AP, and heart rate (HR) during the static protocol. CSP was increased from 40 to 160 mmHg in 20 mmHg increments, resulting in changes of RSNA, AP, and HR through the carotid sinus baroreflex.

CSP_{40-60} and $CSP_{140-160}$ changes than other CSP changes.

Figure 5 and Table 1 show the average gain and phase ($n = 8$) in the neural arc (a), peripheral arc (b), total loop (c), and cardiac baroreflex (d). In the neural arc, $G_{0.04}$ (2.42 ± 0.07 a.u./mmHg) at the CSP_{80-100} change was the highest among all CSP changes, and was almost four to five times higher than those at the CSP_{40-60} (0.54 ± 0.09, $p < 0.01$) and $CSP_{140-160}$ (0.62 ± 0.06, $p < 0.01$) changes. Slopes increased significantly at lower and higher CSP changes compared with the $CSP_{100-120}$ change. Lag time at CSP_{80-100} was the shortest among all CSP changes. In the peripheral arc, Slope and lag time did not differ significantly among the CSP changes, whereas $G_{0.04}$ showed a tendency to decrease slightly with increase of CSP. In the total baroreflex, $G_{0.04}$ at CSP_{80-100} change (1.28 ± 0.12) was significantly higher compared to other CSP changes. Slopes were significantly greater at CSP changes within 60–120 mmHg than other CSP changes. Lag time did not differ significantly among CSP changes. In the cardiac baroreflex, $G_{0.04}$ (0.90 ± 0.18 and 0.92 ± 0.19 beats/min/mmHg) and Slopes were significantly higher at CSP_{80-100} and $CSP_{100-120}$ changes than other CSP changes. There were no significant differences in lag time among CSP changes.

Static Baroreflex

The static characteristics of the total loop were averaged ($n = 8$). Regression analysis was performed for logistic functions. Response range, coefficient of gain, midpoint of input axis, and minimum value of output were 0.45, 0.11, 99.6, and 0.55 in the neural arc, 65.2, 0.07, 97.6, and 69.4 in the total loop, and 29.5, 0.11, 98.2, and 281.2 in the cardiac baroreflex. Linear regression analysis was performed in the peripheral arc (static gain = 0.0086 and offset pressure = 0.027). The intersection between the CSP-AP curve and the line of identity corresponds to AP_{OP} (94.3 mmHg) located in the steepest portion (80–100 mmHg) of the sigmoid

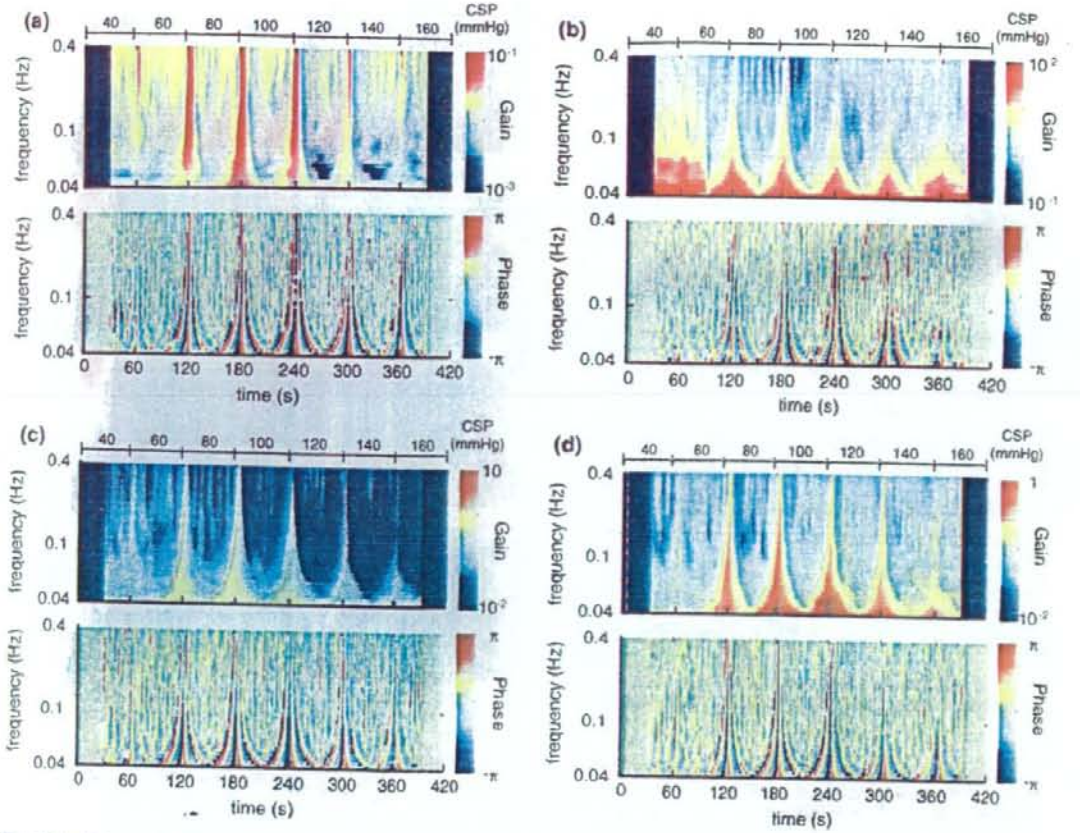

FIGURE 4. Time course of transfer functions of the neural arc from CSP to RSNA (a), peripheral arc from RSNA to AP (b), total baroreflex loop from CSP to AP (c), and cardiac baroreflex from CSP to HR (d) averaged across all animals ($n = 8$).

curve. In the equilibrium diagram, RSNA decreased with increasing CSP in the neural arc, AP increased with increasing RSNA in the peripheral arc, and the intersection between the two arcs provided the AP_{OP} (99.7 mmHg). In the cardiac baroreflex, HR decreased with the increase in CSP.

Bezold-Jarisch Reflex

In the total loop and cardiac baroreflex, the gains at various CSP changes during the BJR were identified ($n = 8$, Fig. 6 and Table 2). Averages of gain and phase (Fig. 6d) were derived from the time series in Figs. 6b and 6c. At middle CSP change of the total loop, $G_{0.04}$ was approximately halved under PBG condition compared to Control (0.59 ± 0.09 vs. 1.39 ± 0.15, $p < 0.01$). Slope and lag time did not differ significantly between the PBG and Control conditions at all CSP changes. In the cardiac baroreflex (Fig. 6e), $G_{0.04}$ tended to modulate under PBG condition at low and high CSP changes, but did not differ significantly between the two conditions at middle CSP changes. Slope differed significantly between the two conditions at low CSP change whereas lag time did not differ significantly at all CSP changes.

Cardiac Baroreflex

The ratio of the cardiac baroreflex to the total loop in dynamic characteristics was studied (Fig. 7). For CSP changes within 60–120 mmHg under Control condition, the ratios were almost linear and increased slightly with increase in frequency; in lower or higher CSP changes, they were modulated especially around 0.2 Hz. For CSP changes under PBG condition, overall the ratios were higher than those under Control condition. For CSP changes within 80–120 mmHg under PBG condition, the ratios were almost linear and the slopes were greater than those of Control condition; in lower or higher CSP changes, they

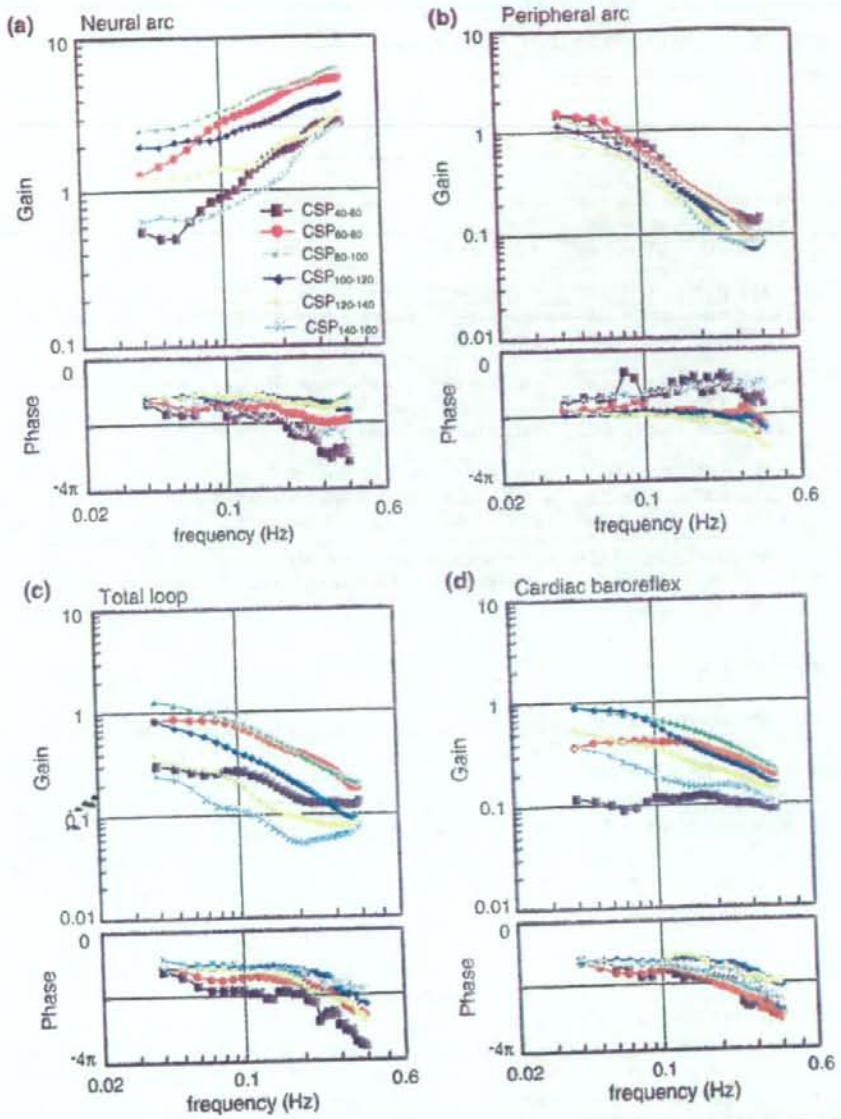

FIGURE 5. Transfer functions of the neural arc from CSP to RSNA, effective peripheral arc from RSNA to AP, total baroreflex loop from CSP to AP, and cardiac baroreflex estimated by wavelet analysis. Average (n = 8) gain (*top*) and phase (*bottom*).

increased within the 0.1–0.2 Hz range and decreased at higher frequencies. The phase difference did not differ among CSP changes under both Control and PBG conditions.

Closed-Loop Baroreflex

Simulation was performed using a cardiac baroreflex system from closed-loop AP input to HR output (Fig. 8a). To test the proposed wavelet analysis, an external disturbance to AP (AP_{noise} = +20 mmHg) was added to the system, and HR responses under carotid sinus open- and closed-loop AP responses were calculated (Fig. 8b). The observed AP and HR (AP_{change} and HR_{change}) were modulated by closed-loop regulation of AP. The CSP is identical with the observed AP_{change}. Gain and phase in the time series (Fig. 8c) and extracted (Fig. 8d) transfer functions were accurately estimated under open and closed AP responses.

TABLE 1. Parameters of the transfer functions in the neural arc, peripheral arc, total loop, and cardiac baroreflex at various step pressure inputs.

	CSP (mmHg)					
	40–60	60–80	80–100	100–120	120–140	140–160
Neural arc						
$G_{0.04}$ (a.u./mmHg)	0.54 ± 0.09	1.25 ± 0.17**	2.42 ± 0.07**,††	1.89 ± 0.13**,†	1.18 ± 0.20*,‡‡,¶¶	0.62 ± 0.06†,‡‡,**
Slope (dB/decade)	17.9 ± 4.1	10.0 ± 1.9	7.7 ± 2.0	5.8 ± 3.1*	11.0 ± 1.8	16.8 ± 3.1*
Lag time (s)	2.63 ± 0.58	0.78 ± 0.16*	0.27 ± 0.18**	0.48 ± 0.14**	0.45 ± 0.17**	1.83 ± 0.71
Peripheral arc						
$G_{0.04}$ (mmHg/a.u.)	1.42 ± 0.17	1.50 ± 0.18	1.30 ± 0.08	1.13 ± 0.13	0.85 ± 0.10†	0.92 ± 0.09†
Slope (dB/decade)	−24.6 ± 3.3	−29.4 ± 1.3	−28.2 ± 0.8	−26.6 ± 2.8	−22.7 ± 2.8	−23.2 ± 4.6
Lag time (s)	0.40 ± 0.79	1.29 ± 0.20	1.35 ± 0.20	1.35 ± 0.58	2.10 ± 0.69	0.08 ± 0.64
Total loop						
$G_{0.04}$	0.29 ± 0.05	0.85 ± 0.16**	1.28 ± 0.12**,††	0.83 ± 0.09**,‡‡	0.38 ± 0.07††,‡‡,¶¶	0.24 ± 0.04††,‡‡,**
Slope (dB/decade)	−6.8 ± 4.1	−19.4 ± 2.4**	−20.5 ± 1.6**	−20.7 ± 2.1**	−11.8 ± 2.7	−6.4 ± 4.1††,‡‡,**
Lag time (s)	3.03 ± 0.61	2.07 ± 0.12	1.62 ± 0.20	1.82 ± 0.60	2.54 ± 0.62	1.91 ± 0.41
Cardiac baroreflex						
$G_{0.04}$ (beats/min/mmHg)	0.11 ± 0.02	0.37 ± 0.11	0.90 ± 0.18**,††	0.92 ± 0.19**,††	0.55 ± 0.12**,‡,¶	0.36 ± 0.09‡‡,¶¶
Slope (dB/decade)	−2.3 ± 2.1	−10.7 ± 2.3	−15.9 ± 2.8**	−19.0 ± 2.9**	−11.8 ± 2.6	−6.3 ± 3.1‡,**
Lag time (s)	2.13 ± 0.62	2.26 ± 0.34	2.17 ± 0.62	1.51 ± 0.16	1.70 ± 0.61	1.92 ± 0.86

$G_{0.04}$, transfer gain at 0.04 Hz. Slope, average slope of transfer gain between 0.1 and 0.4 Hz.
$p < 0.01$; ** vs. 40–60, †† vs. 60–80, ‡‡ vs. 80–100, and ¶¶ vs. 100–120 mmHg in CSP change; the same symbols of a single show $p < 0.05$.

DISCUSSION

We have shown that the analysis using wavelet transform can identify the dynamic baroreflex properties at various pressure levels from the time-course data under normal (Fig. 5) and pathophysiological conditions (Fig. 6) with background noise. The results of the proposed analysis applied in animal experiments indicate the possibility of its use in the assessment of human baroreflex (Figs. 7 and 8).

Time-Series Analysis for Dynamic Baroreflex

Under the background noise added to the response model, the proposed analysis applied to step response was able to detect the dynamic baroreflex characteristics (Fig. 2). The standard spectral analysis under stationary conditions has high reliability in the baroreflex test, and uses longer data to cancel the noise[31,38] at various pressure inputs and lose the short-term and important changes. In direct calculation of the dynamic characteristics from the step input output data, the traditional time series analysis might also have a disadvantage under noise contamination, which may cause poor S/N ratio in the impaired baroreflex function of cardiac diseases.[41] The STFFT using time windows of a constant range for all frequencies was actually unable to catch the dynamic property especially at higher frequencies under such condition (Figs. 1 and 2d) because of the average one within the whole time window. On the other hand, the modified wavelet-based analysis with improved temporal resolution at higher frequencies to reasonably catch the localized changes in cardiovascular control[4,50] will be effective for extracting the dynamic baroreflex characteristics under nonstationary hemodynamics with a low S/N ratio. Because the baroreflex test may depend on the various S/N ratios depending on the system input (e.g. amplitude) and/or the background noises, further investigations will be required in this regard.

Burgess *et al.*[2] showed that cross spectrum analysis using wavelet transform characterized strong coupling between sympathetic nerve traffic and AP at frequencies of <0.1 Hz. Davrath *et al.*[4] reported that time-varying power obtained from wavelet transform of the spontaneous HR or AP fluctuation in humans are remarkably modulated at approximately 0.1 Hz under standing condition. Whereas the traditional wavelet analysis could extract the localized characteristics of time-series data in a nonstationary condition,[2,4] application to dynamic system identification is difficult because of the limitation in phase extraction. When the same time window is set for the input and output data, the actual information of phase and gain may be lost or split, instead of high temporal resolution of wavelet transform.[34] To apply wavelet analysis to the baroreflex system identification, we expanded the basic analysis by acquiring the transfer function from maximum input and output data. The proposed method was able to acquire the system identification of baroreflex because of the specific characteristics of wavelet

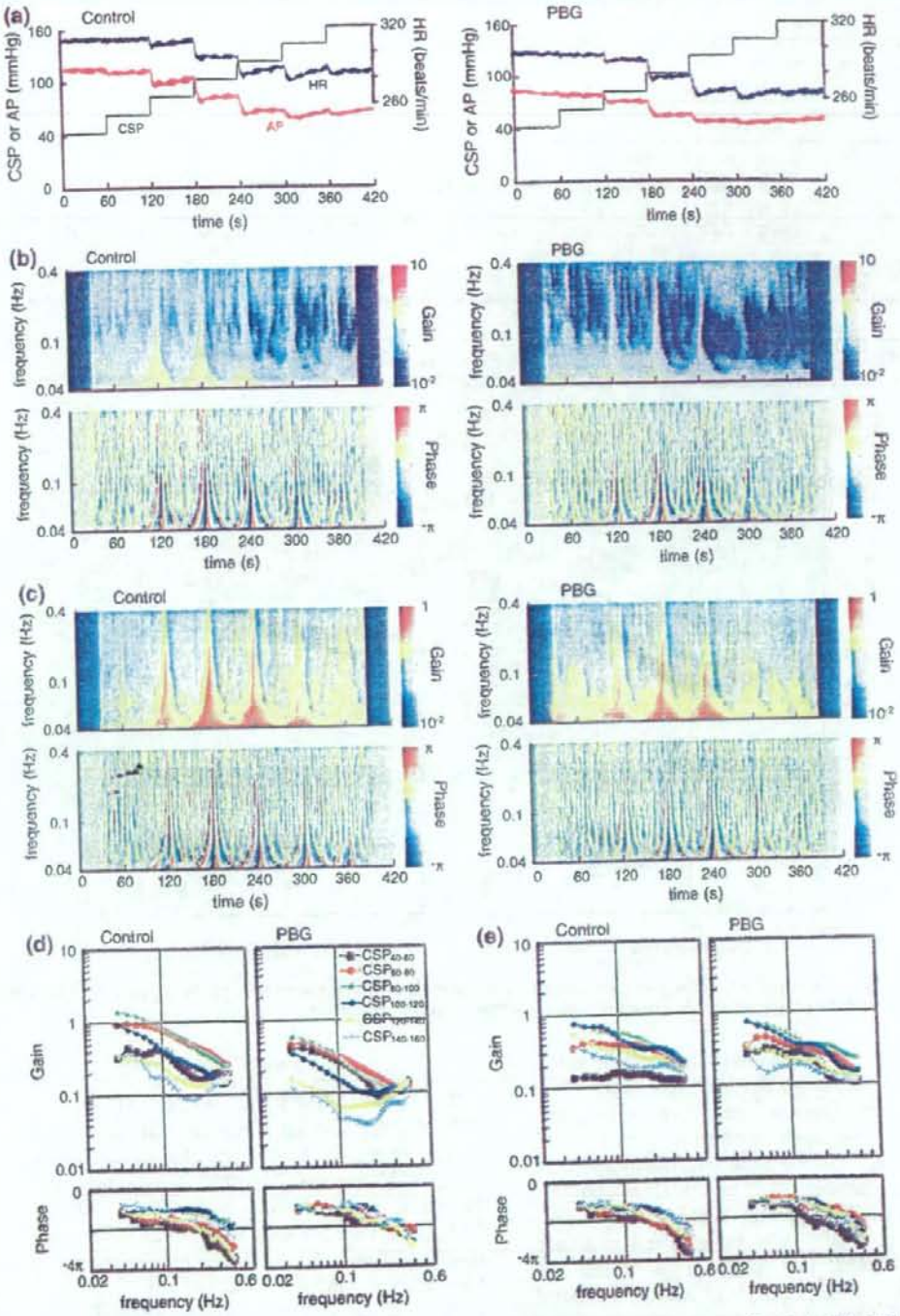

FIGURE 6. (a) Averaged (n = 8) time series of CSP, AP, and HR obtained in the absence (Control, *left*) and presence of phenylbiguanide (PBG, *right*). CSP was increased from 40 to 160 mmHg in 20 mmHg increments, resulting in changes in AP and HR through the carotid sinus baroreflex. Time-series transfer functions of total loop (b) and cardiac baroreflex (c) in the Control (*left*) and PBG (*right*) conditions. Average (n = 8) gain (*top*) and phase (*bottom*). Transfer functions of total loop (d) and cardiac baroreflex (e) estimated by wavelet analysis in the Control (*left*) and PBG (*right*) conditions.

TABLE 2. Parameters of the transfer functions for the total loop and cardiac baroreflex before and during PBG infusion.

	Low CSP (40–60 mmHg)		Middle CSP (80–100 mmHg)		High CSP (120–140 mmHg)	
	Control	PBG	Control	PBG	Control	PBG
Total loop						
$G_{0.04}$	0.32 ± 0.07	0.39 ± 0.09††	1.39 ± 0.15	0.59 ± 0.09**,††	0.35 ± 0.04††	0.15 ± 0.02††
Slope (dB/decade)	−11.6 ± 3.3	−8.0 ± 4.2	−17.8 ± 2.1	−15.0 ± 3.2	−6.5 ± 2.5	7.4 ± 5.3††
Lag time (s)	2.90 ± 0.71	1.43 ± 0.68	1.44 ± 0.22	2.21 ± 0.59	3.48 ± 0.61	2.74 ± 0.89
Cardiac baroreflex						
$G_{0.04}$ (beats/min/mmHg)	0.14 ± 0.02	0.26 ± 0.10†	0.78 ± 0.21	0.75 ± 0.18	0.54 ± 0.13	0.35 ± 0.08†
Slope (dB/decade)	−1.8 ± 2.2	−12.5 ± 2.9*	−13.4 ± 2.7	−11.6 ± 2.1	−12.6 ± 2.7	−6.6 ± 4.0
Lag time (s)	2.99 ± 0.89	2.91 ± 0.55	2.06 ± 0.30	2.28 ± 0.54	2.65 ± 0.72	2.47 ± 0.77

$G_{0.04}$, transfer gain at 0.04 Hz. Slope, average slope of gain between 0.1 and 0.4 Hz. PBG, phenylbiguanide.
** $p < 0.01$ and * $p < 0.05$, PBG vs. Control at the same CSP; †† $p < 0.01$ and † $p < 0.05$, all conditions vs. CSP_{80-100} of Control.

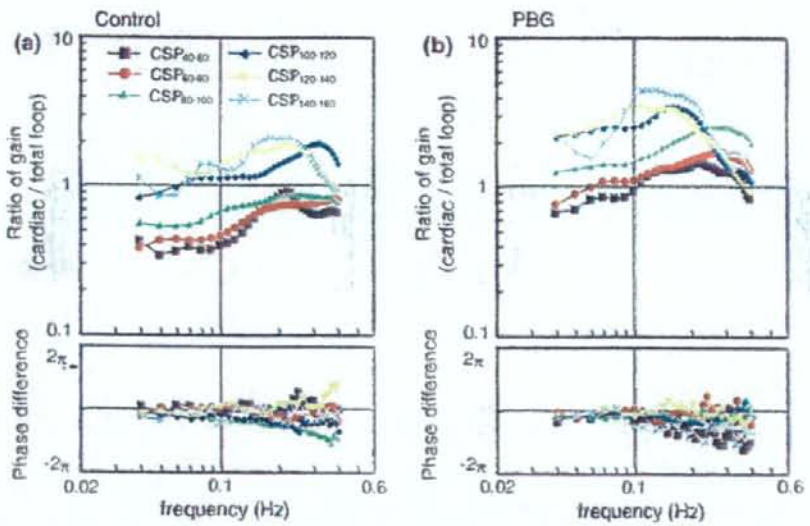

FIGURE 7. The ratio in the transfer functions of the cardiac baroreflex (CSP-HR) to the total loop (CSP-AP) ($n = 8$). The ratio of dynamic gain (*top*) and the phase difference (*bottom*). Control (a) and PBG (b) conditions.

transform that can adjust the analysis window at every frequency level and extract the localized data. When the mother wavelet is appropriately used for any purpose, the fields of the application of wavelet analysis might be extended. We used the traditional and reasonable Morlet function;[11,48,49] however, the comparison with other wavelet functions such as Mexican hat, Haar, and Daubechies[34] will be required in future studies. In addition, the convolutions within the transfer function of Eq. (3) may lose the temporal information; however, because the wavelet transform reflects the effect of reasonably changed time window, the gain and phase updated every 0.2 s can continuously express the representative property at the center point of the time window during the time-course change.

Physiological Perspective

The powers of the RSNA, AP, and HR responses to CSP changes showed maximum values at CSP_{80-100} change (Fig. 3b), which was almost consistent with AP_{OP} (94.3 and 99.7 mmHg) from static analysis. In contrast, the power responses at CSP_{40-60} and $CSP_{140-160}$ changes were lower than those at AP_{OP}, resulting from the nonlinear characteristics of the baroreflex around threshold and saturation to AP inputs as indicated by the static analysis. The gain and phase were revealed within the physiological range including nonlinear points in normal rabbits (Figs. 4 and 5). Whereas the static analysis cannot show the dynamic characteristics at higher frequencies (e.g. > 0.01 Hz[18]), the proposed wavelet-based analysis

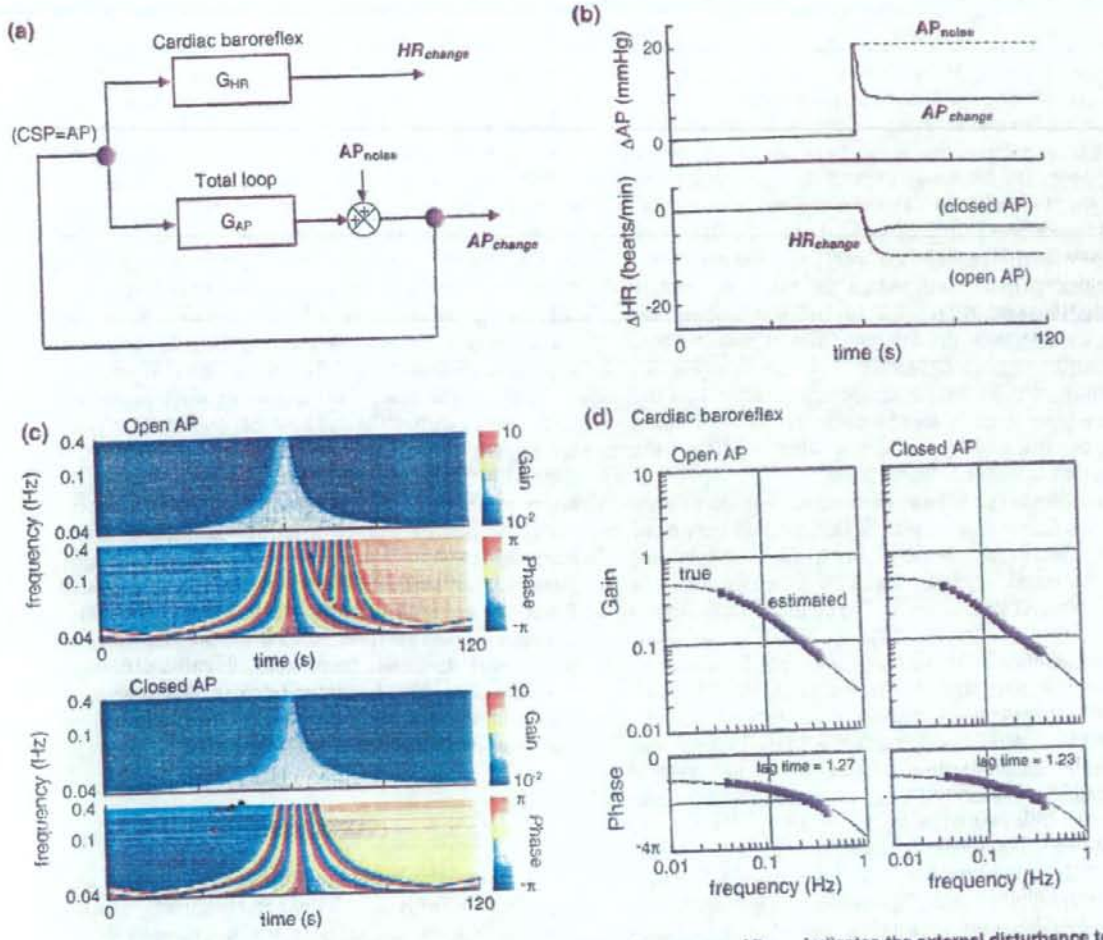

FIGURE 8. (a) Block diagram of cardiac baroreflex under closed-loop AP response. AP_{noise} indicates the external disturbance to AP. AP_{change} and HR_{change} show the actual changes of AP and HR. G_{AP} and G_{HR} are transfer functions under open loop responses in the total loop and cardiac baroreflex. (b) AP_{noise} of +20 mmHg as input and AP_{change} as output under the closed loop (*top*). HR responses under the open- and closed-loop AP changes (*bottom*). (c) Time-series transfer functions of cardiac baroreflex under open- and closed-loop AP changes. (d) Transfer functions of cardiac baroreflex estimated under the open (*left*) and closed (*right*) AP responses. Gain (*top*) and phase (*bottom*). Dotted lines, theoretical values. Squares, estimated values by our wavelet analysis.

could derive them from the same step input protocol, which may be able to reduce the number of experiments and duration of data acquisition.

Clinical Implications for Cardiac Patients

The wavelet-based system identification indicated a possibility to acquire pathophysiological understanding under various responses with cardiac diseases. The proposed analysis revealed that the dynamic characteristics in the total loop and neural arc were significantly attenuated at various pressure changes containing nonlinear points under PBG condition (Fig. 6 and Table 2), in addition to the previous studies.[18,20] The $G_{0.04}$ at AP_{OP} in Control (1.39 ± 0.15) was decreased to almost half during PBG condition (0.59 ± 0.09); it was attenuated to 1/3–1/4 times as small as that under PBG condition (0.39 ± 0.09) at low CSP_{40-60} change, which may be induced by the decrease of peripheral pump function in heart failure, suggesting the risk of further bluntness of baroreflex ability during the BJR.

In carotid-cardiac response, HR may be related to the assessment of AP regulation by the product of HR, stroke volume, and total peripheral resistance, rather than RR interval.[7,8] Because it may be difficult to evaluate the baroreflex to regulate AP under the carotid-sinus closed loop condition (i.e. CSP = AP), we

explored the possibility to evaluate the baroreflex dynamics from the HR response related to AP regulation, considering the dissociation between animal and human studies and applying the proposed method. The transfer functions of the cardiac baroreflex were similar to those of the total loop around the operating point (Fig. 7a). On the other hand, the dynamic characteristics in nonlinear CSP points and during the BJR were greater than those around the operating point in Control condition (Fig. 7b), suggesting the effect of cardiac sympathovagal activity. Next, to consider human baroreflex assessment, the dynamic transfer function was estimated by the closed-loop model response (Fig. 8), resulting in the effective assessment. Even when the system input is modulated by the nature of closed-loop response, it would be crucial to be able to estimate the dynamic baroreflex characteristics.

The spontaneous baroreflex method is commonly used in clinical assessments.[37] This method may have some limitations because of the highly complex and interconnected cardiovascular mechanisms in short-term AP regulation[27,40,43] and the unclear system input might induce the different pathophysiological understandings.[42] On the other hand, our focus was to explore the possibility of the evaluation of the baroreflex to regulate AP against great external disturbances in patients with cardiovascular diseases and unstable hemodynamics. To identify the system dynamics of the carotid-sinus baroreflex for AP regulation with sympathovagal activity,[51] this study improved the standard analyses, particularly considering the pure time delay. Using the transfer function corresponding to the independent step input frequency, the proposed analysis was able to indicate some novel aspects of the dynamic baroreflex properties during the BJR as mentioned above.

For clinical application, the other indexes (e.g. AP to muscle SNA response[14]) for AP regulation might be tested. In addition, in the time-course data, there are some effective methods such as complex demodulation method[13] based on the low pass filter, focusing on a frequency band such as LF and HF; it has good temporal resolution. However, the complex demodulation method might concentrate on the information of amplitude in a frequency band, not on each frequency level within the band. This limitation makes it impossible to perform the system identification in this study to reproduce the response corresponding to a wide frequency. Furthermore, the continuous estimation of the dynamics might connect to an effective index of the real-time control of hemodynamics such as an automated drug infusion system.[17,19]

Because we kept the bilateral vagi intact, low pressure baroreflexes from the cardiopulmonary region might have interacted with the arterial baroreflex, affecting estimation of carotid sinus baroreflex transfer functions. After the vagotomy, the dynamics from isolated aortic depressor nerve to AP responses was almost preserved and AP remained unchanged despite a HR decrease.[28,46] Our previous data of dynamic baroreflex properties with[20] and without[21] vagal nerves were compared. The dynamic characteristics of the total loop and cardiac baroreflex around the operating point were similar, whereas the corner frequency was slightly greater under intact vagal condition. Next, the static gain may be increased during the rising pressure protocol, compared with the falling one.[46] Hysteresis induced by the rising and falling pressure protocols may also modulate the dynamic baroreflex. However, the vagal effect of the cardiovascular receptors on the dynamics may not be large.[28] Third, the phases at lower or higher CSP changes in the transfer functions varied with the observed frequency because of nonlinear characteristics in the neural arc and the input power in the peripheral arc decreased by the neural arc. Especially at high frequencies, the phases appear to be modulated because of the step input showing low power with the high frequency. Finally, the simple models used for the simulations in this study have some limitations, such as a lack of information of nonparametric components or nonlinearity.[23]

CONCLUSIONS

The wavelet-based time-frequency analysis was capable of identifying the dynamic baroreflex properties over wide frequencies at various pressure levels both in normal and BJR conditions. Because the dynamic baroreflex properties to physiological pressure inputs as well as static characteristics can be simultaneously extracted from the short-term responses with background noise, the proposed method is potentially applicable to assess human dynamic baroreflex function under carotid-sinus closed-loop condition.

APPENDIX

Model Response of Arterial Baroreflex

We used the following model[15] as the carotid sinus open loop baroreflex for the simulation study (Figs. 1 and 2). The neural arc transfer function [$G_N(f)$] using a first-order high-pass filter can be expressed as

$$G_N(f) = -K_N\left(1 + \frac{f}{f_C}i\right)\exp(-2\pi f i L_N)$$

where f and i represent the frequency (Hz) and imaginary units, respectively; K_N is the neural arc gain; f_C is the frequency (Hz) for a derivative characteristic; L_N is lag time (s).

The peripheral arc transfer function $[G_P(f)]$ using a second-order low-pass filter can be expressed as

$$G_P(f) = \frac{K_P}{1 + 2\zeta\frac{f}{f_N}i + \left(\frac{f}{f_N}i\right)^2} \exp(-2\pi f i L_P)$$

where K_P, f_N, ζ, and L_P represent the peripheral arc gain, natural frequency (Hz), damping ratio, and lag time (s), respectively.

The transfer function of the total baroreflex loop is expressed as the product of the neural and peripheral arc transfer functions.

$$G_{AP}(f) = G_N(f) \cdot G_P(f)$$

The gain and lag time of the total baroreflex loop is expressed as $K = K_N \cdot K_P$ and $L = L_N + L_P$. The parameters of the model response were set at $K = 1.0$, $f_C = 0.12$, $L_N = 0.55$, $f_N = 0.071$, $\zeta = 1.37$, and $L_P = 1.0$ according to previous data.[15]

Model of Baroreflex Under Closed-Loop AP Response

The baroreflex system under the closed-loop AP input to HR response was modeled (Fig. 8a).

$$HR_{change}(f) = G_{HR}(f) \cdot AP_{change}(f)$$

The pressure change $[AP_{change}(f)]$ to the exogenous perturbation $[AP_{noise}(f)]$ is the sum of the feedback signal and perturbation under closed-loop condition.[15] G_{HR} is the transfer function under the carotid sinus open loop in the cardiac baroreflex (CSP input and HR output).

$$AP_{change}(f) = G_{AP}(f) \cdot AP_{change}(f) + AP_{noise}(f)$$

Rearranging above equation with respect to $AP_{change}(f)$ yields

$$AP_{change}(f) = \frac{AP_{noise}(f)}{1 - G_{AP}(f)}$$

The time integral of the inverse Fourier transform of $AP_{change}(f)$ is the AP change to an exogenous step perturbation. G_{AP} is the transfer function under the carotid sinus open loop for the total baroreflex. The AP_{change} and HR_{change} can be simply observed by the monitoring system. The transfer function between the HR and AP responses was excluded because of the insignificant relationship as previously indicated.[22]

The transfer functions, G_{AP} and G_{HR}, were approximated using a first-order low-pass filter.

$$G(f) = \frac{-K}{\left(1 + \frac{f}{f_C}i\right)} \cdot \exp(-2\pi f i L)$$

The parameters of the transfer functions were set at $K = 1.03$, $f_C = 0.018$, and $L = 1.34$ for the total loop (Fig. 8a, G_{AP}); $K = 0.51$, $f_C = 0.049$, and $L = 1.14$ for the cardiac baroreflex (G_{HR}), according to previous data.[20]

ACKNOWLEDGMENTS

This study was supported by "Health and Labour Sciences Research Grant for Research on Advanced Medical Technology", "Health and Labour Sciences Research Grant for Research on Medical Devices for Analyzing, Supporting and Substituting the Function of Human Body", "Health and Labour Sciences Research Grant H18-Iryo-Ippan-023" from the Ministry of Health, Labour and Welfare of Japan, "Program for Promotion of Fundamental Studies in Health Science" from the National Institute of Biomedical Innovation, and "a Grant-in-Aid for Young Scientists (B)" from the Ministry of Education, Culture, Sports, Science and Technology of Japan (KAKENHI, 20700392).

REFERENCES

[1]Ando, S., H. R. Dajani, B. L. Senn, G. E. Newton, and J. S. Floras. Sympathetic alternans. Evidence for arterial baroreflex control of muscle sympathetic nerve activity in congestive heart failure. *Circulation* 95:316–319, 1997.

[2]Burgess, D. E., D. C. Randall, R. O. Speakman, and D. R. Brown. Coupling of sympathetic nerve traffic and BP at very low frequencies is mediated by large-amplitude events. *Am. J. Physiol. Regul. Integr. Comp. Physiol.* 284:R802–R810, 2003.

[3]Dampney, R. A. Functional organization of central pathways regulating the cardiovascular system. *Physiol. Rev.* 74:323–364, 1994.

[4]Davrath, L. R., Y. Goren, I. Pinhas, E. Toledo, and S. Akselrod. Early autonomic malfunction in normotensive individuals with a genetic predisposition to essential hypertension. *Am. J. Physiol. Heart Circ. Physiol.* 285:H1697–H1704, 2003.

[5]Eckberg, D. L., and T. A. Kuusela. Human vagal baroreflex sensitivity fluctuates widely and rhythmically at very low frequencies. *J. Physiol.* 567:1011–1019, 2005. doi:10.1113/jphysiol.2005.091090.

[6]Ellenbogen, K. A., P. K. Mohanty, S. Szentpetery, and M. D. Thames. Arterial baroreflex abnormalities in heart failure: reversal after orthotopic cardiac transplantation. *Circulation* 79:51–58, 1989.

[7]Fadel, P. J., S. Ogoh, D. M. Keller, and P. B. Raven. Recent insights into carotid baroreflex function in humans

using the variable pressure neck chamber. *Exp. Physiol.* 88:671–680, 2003. doi:10.1113/eph8802650.

[8]Fadel, P. J., M. Stromstad, D. W. Wray, S. A. Smith, P. B. Raven, and N. H. Secher. New insights into differential baroreflex control of heart rate in humans. *Am. J. Physiol. Heart Circ. Physiol.* 284:H735–H743, 2003.

[9]Glantz, S. A. Primer of Biostatistics. 4th ed. New York: McGraw Hill, 1997.

[10]Grassi, G., C. Turri, G. Seravalle, G. Bertinieri, A. Pierini, and G. Mancia. Effects of chronic clonidine administration on sympathetic nerve traffic and baroreflex function in heart failure. *Hypertension* 38:286–291, 2001. doi:10.1161/hy1201.096117.

[11]Grossmann, A., R. Kronland-Martinet, and J. Morlet. Reading and understanding continuous wavelets transforms. In: Wavelets, Time-Frequency Methods and Phase Space, edited by J. M. Combes, A. Grossmann, and P. Tchamitchian. Berlin: Springer, 1989, pp. 2–20.

[12]Guyton, A. C., T. G. Coleman, and H. J. Granger. Circulation: overall regulation. *Annu. Rev. Physiol.* 34:13–46, 1972. doi:10.1146/annurev.ph.34.030172.000305.

[13]Hayano, J., J. A. Taylor, S. Mukai, A. Okada, Y. Watanabe, K. Takata, and T. Fujinami. Assessment of frequency shifts in R-R interval variability and respiration with complex demodulation. *J. Appl. Physiol.* 77:2879–2888, 1994.

[14]Ichinose, M., M. Saito, N. Kondo, and T. Nishiyasu. Time-dependent modulation of arterial baroreflex control of muscle sympathetic nerve activity during isometric exercise in humans. *Am. J. Physiol. Heart Circ. Physiol.* 290:H1419–H1426, 2006. doi:10.1152/ajpheart.00847.2005.

[15]Ikeda, Y., T. Kawada, M. Sugimachi, O. Kawaguchi, T. Shishido, T. Sato, H. Miyano, W. Matsuura, J. Alexander, Jr., and K. Sunagawa. Neural arc of baroreflex optimizes dynamic pressure regulation in achieving both stability and quickness. *Am. J. Physiol. Heart Circ. Physiol.* 271:H882–H890, 1996.

[16]Jordan, J., H. R. Toka, K. Heusser, O. Toka, J. R. Shannon, J. Tank, A. Diedrich, C. Stabroth, M. Stoffels, R. Naraghi, W. Oelkers, H. Schuster, H. P. Schobel, H. Haller, and F. C. Luft. Severely impaired baroreflex-buffering in patients with monogenic hypertension and neurovascular contact. *Circulation* 102:2611–2618, 2000.

[17]Kashihara, K. Automatic regulation of hemodynamic variables in acute heart failure by a multiple adaptive predictive controller based on neural networks. *Ann. Biomed. Eng.* 34:1846–1869, 2006. doi:10.1007/s10439-006-9190-9.

[18]Kashihara, K., T. Kawada, M. Li, M. Sugimachi, and K. Sunagawa. Bezold-Jarisch reflex induced by phenylbiguanide lowers arterial pressure mainly via the downward shift of the baroreflex neural arc. *Jpn. J. Physiol.* 54:395–404, 2004. doi:10.2170/jjphysiol.54.395.

[19]Kashihara, K., T. Kawada, K. Uemura, M. Sugimachi, and K. Sunagawa. Adaptive predictive control of arterial blood pressure based on a neural network during acute hypotension. *Ann. Biomed. Eng.* 32:1365–1383, 2004. doi:10.1114/B:ABME.0000042225.19806.34.

[20]Kashihara, K., T. Kawada, Y. Yanagiya, K. Uemura, M. Inagaki, H. Takaki, M. Sugimachi, and K. Sunagawa. Bezold-Jarisch reflex attenuates dynamic gain of baroreflex neural arc. *Am. J. Physiol. Heart Circ. Physiol.* 285:H833–H840, 2003.

[21]Kashihara, K., Y. Takahashi, K. Chatani, T. Kawada, C. Zheng, M. Li, M. Sugimachi, and K. Sunagawa. Intravenous angiotensin II does not affect dynamic baroreflex characteristics of the neural or peripheral arc. *Jpn. J. Physiol.* 53:135–143, 2003. doi:10.2170/jjphysiol.53.135.

[22]Kawada, T., T. Miyamoto, K. Uemura, K. Kashihara, A. Kamiya, M. Sugimachi, and K. Sunagawa. Effects of neuronal norepinephrine uptake blockade on baroreflex neural and peripheral arc transfer characteristics. *Am. J. Physiol. Regul. Integr. Comp. Physiol.* 286:R1110–1120, 2004. doi:10.1152/ajpregu.00527.2003.

[23]Kawada, T., Y. Yanagiya, K. Uemura, T. Miyamoto, C. Zheng, M. Li, M. Sugimachi, and K. Sunagawa. Input-size dependence of the baroreflex neural arc transfer characteristics. *Am. J. Physiol. Heart Circ. Physiol.* 284:H404–H415, 2003.

[24]Kent, B. B., J. W. Drane, B. Blumenstein, and J. W. Manning. A mathematical model to assess changes in the baroreceptor reflex. *Cardiology* 57:295–310, 1972.

[25]Landesberg, G., D. Adam, Y. Berlatzky, and S. Akselrod. Step baroreflex response in awake patients undergoing carotid surgery: time- and frequency-domain analysis. *Am. J. Physiol.* 274:H1590–H1597, 1998.

[26]Lee, D. Coherent oscillations in neuronal activity of the supplementary motor area during a visuomotor task. *J. Neurosci.* 23:6798–6809, 2003.

[27]Lipman, R. D., J. K. Salisbury, and J. A. Taylor. Spontaneous indices are inconsistent with arterial baroreflex gain. *Hypertension* 42:481–487, 2003. doi:10.1161/01.HYP.0000091370.83602.E6.

[28]Liu, H. K., S. J. Guild, J. V. Ringwood, C. J. Barrett, B. L. Leonard, S. K. Nguang, M. A. Navakatikyan, and S. C. Malpas. Dynamic baroreflex control of blood pressure: influence of the heart vs. peripheral resistance. *Am. J. Physiol. Regul. Integr. Comp. Physiol.* 283:R533–R542, 2002.

[29]Lucini, D., M. Pagani, G. S. Mela, and A. Malliani. Sympathetic restraint of baroreflex control of heart period in normotensive and hypertensive subjects. *Clin. Sci. (Lond.)* 86:547–556, 1994.

[30]Malliani, A., M. Pagani, F. Lombardi, and S. Cerutti. Cardiovascular neural regulation explored in the frequency domain. *Circulation* 84:482–492, 1991.

[31]Marmarelis, P. Z., and V. Z. Marmarelis. The white noise method in system identification. In: Analysis of Physiological Systems. New York: Plenum, 1978, pp. 131–221.

[32]Masaki, H., T. Imaizumi, Y. Harasawa, and A. Takeshita. Dynamic arterial baroreflex in rabbits with heart failure induced by rapid pacing. *Am. J. Physiol.* 267:H92–H99, 1994.

[33]Mohrman, D. E., and L. J. Heller. Cardiovascular Physiology. 4th ed. New York: McGraw-Hill, 1997.

[34]Motard, R. L., and B. Joseph. Wavelet Applications in Chemical Engineering. Boston: Kluwer Academic Publishers, 1994.

[35]Munakata, M., Y. Imai, H. Takagi, M. Nakao, M. Yamamoto, and K. Abe. Altered frequency-dependent characteristics of the cardiac baroreflex in essential hypertension. *J. Auton. Nerv. Syst.* 49:33–45, 1994. doi:10.1016/0165-1838(94)90018-3.

[36]Osculati, G., G. Grassi, C. Giannattasio, G. Seravalle, F. Valagussa, A. Zanchetti, and G. Mancia. Early alterations of the baroreceptor control of heart rate in patients with acute myocardial infarction. *Circulation* 81:939–948, 1990.

[37]Parati, G., M. DiRienzo, and G. Mancia. Dynamic modulation of baroreflex sensitivity in health and disease. *Ann. NY Acad. Sci.* 940:469–487, 2001.

[38]Parati, G., J. P. Saul, and P. Castiglioni. Assessing arterial baroreflex control of heart rate: new perspectives. *J. Hypertens.* 22:1259–1263, 2004. doi:10.1097/01.hjh.0000125469.35523.32.

[39]Parmer, R. J., J. H. Cervenka, and R. A. Stone. Baroreflex sensitivity and heredity in essential hypertension. *Circulation* 85:497–503, 1992.

[40]Persson, P. B., M. DiRienzo, P. Castiglioni, C. Cerutti, M. Pagani, N. Honzikova, S. Akselrod, and G. Parati. Time versus frequency domain techniques for assessing baroreflex sensitivity. *J. Hypertens.* 19:1699–1705, 2001. doi:10.1097/00004872-200110000-00001.

[41]Pinna, G. D., R. Maestri, G. Raczak, and M. T. La Rovere. Measuring baroreflex sensitivity from the gain function between arterial pressure and heart period. *Clin. Sci. (Lond.)* 103:81–88, 2002.

[42]Pitzalis, M. V., F. Mastropasqua, A. Passantino, F. Massari, L. Ligurgo, C. Forleo, C. Balducci, F. Lombardi, and P. Rizzon. Comparison between noninvasive indices of baroreceptor sensitivity and the phenylephrine method in post-myocardial infarction patients. *Circulation* 97:1362–1367, 1998.

[43]Porta, A., G. Baselli, O. Rimoldi, A. Malliani, and M. Pagani. Assessing baroreflex gain from spontaneous variability in conscious dogs: role of causality and respiration. *Am. J. Physiol. Heart Circ. Physiol.* 279:H2558–H2567, 2000.

[44]Radaelli, A., L. Bernardi, F. Valle, S. Leuzzi, F. Salvucci, L. Pedrotti, E. Marchesi, G. Finardi, and P. Sleight. Cardiovascular autonomic modulation in essential hypertension. Effect of tilting. *Hypertension* 24:556–563, 1994.

[45]Rudas, L., A. A. Crossman, C. A. Morillo, J. R. Halliwill, K. U. Tahvanainen, T. A. Kuusela, and D. L. Eckberg. Human sympathetic and vagal baroreflex responses to sequential nitroprusside and phenylephrine. *Am. J. Physiol.* 276:H1691–H1698, 1999.

[46]Sagawa, K. Baroreflex control of systemic arterial pressure and vascular bed. In: Handbook of Physiology. The Cardiovascular System. Peripheral Circulation and Organ Blood Flow, sect. 2, vol. III, pt. 2, chap. 14. Bethesda, MD: Am. Physiol. Soc., 1983, pp. 453–496.

[47]Sato, T., T. Kawada, M. Inagaki, T. Shishido, H. Takaki, M. Sugimachi, and K. Sunagawa. New analytic framework for understanding sympathetic baroreflex control of arterial pressure. *Am. J. Physiol.* 276:H2251–H2261, 1999.

[48]Sinkkonen, J., H. Tiitinen, and R. Naatanen. Gabor filters: an informative way for analysing event-related brain activity. *J. Neurosci. Methods* 56:99–104, 1995. doi:10.1016/0165-0270(94)00111-S.

[49]Tallon-Baudry, C., O. Bertrand, C. Delpuech, and J. Pernier. Stimulus specificity of phase-locked and non-phase-locked 40 Hz visual responses in human. *J. Neurosci.* 16:4240–4249, 1996.

[50]Toledo, E., O. Gurevitz, H. Hod, M. Eldar, and S. Akselrod. Wavelet analysis of instantaneous heart rate: a study of autonomic control during thrombolysis. *Am. J. Physiol. Regul. Integr. Comp. Physiol.* 284:R1079–R1091, 2003.

[51]Westerhof, B. E., J. Gisolf, J. M. Karemaker, K. H. Wesseling, N. H. Secher, and J. J. van Lieshout. Time course analysis of baroreflex sensitivity during postural stress. *Am. J. Physiol. Heart Circ. Physiol.* 291:H2864–H2874, 2006. doi:10.1152/ajpheart.01024.2005.

[52]Zhang, R., K. Behbehani, C. G. Crandall, J. H. Zuckerman, and B. D. Levine. Dynamic regulation of heart rate during acute hypotension: new insight into baroreflex function. *Am. J. Physiol. Heart Circ. Physiol.* 280:H407–H419, 2001.

PAPER Special Section on Medical Information and Communications Technologies

Position Estimation Method of Medical Implanted Devices Using Estimation of Propagation Velocity inside Human Body

Makoto KAWASAKI[†a)], *Student Member and* Ryuji KOHNO[†b)], *Fellow*

SUMMARY Wireless communication devices in the field of medical implant, such as cardiac pacemakers and capsule endoscopes, have been studied and developed to improve healthcare systems. Especially it is very important to know the range and position of each device because it will contribute to an optimization of the transmission power. We adopt the time-based approach of position estimation using ultra wideband signals. However, the propagation velocity inside the human body differs in each tissue and each frequency. Furthermore, the human body is formed of various tissues with complex structures. For this reason, propagation velocity is different at a different point inside human body and the received signal so distorted through the channel inside human body. In this paper, we apply an adaptive template synthesis method in multipath channel for calculate the propagation time accurately based on the output of the correlator between the transmitter and the receiver. Furthermore, we propose a position estimation method using an estimation of the propagation velocity inside the human body. In addition, we show by computer simulation that the proposal method can perform accurate positioning with a size of medical implanted devices such as a medicine capsule.

key words: *medical implanted device, position estimation, inside human body, ultra wideband, propagation velocity*

1. Introduction

Recently, wireless communication devices in the field of medical implant (cardiac pacemaker and capsule endoscope and so on) are studied extensively towards practical use. In the future, by transmitting vital data from one device to another implanted device in a network of medical implants, we can observe the body's condition and to detect any possible problem in the human body at anytime and anywhere. These can be a great help for doctors to diagnose and to cure diseases [6], [7].

Considering that transmitted information of vital data is highly important and the need for long-lasting batteries, it is important that wireless communications of medical implanted devices to be highly-reliable with low transmission power consumption. In that regard, it is very important to know ranging and position of each device, because that can help to the optimization of the transmission power and to know the position of biological informations obtained from medical implanted device. In this paper, we employ ultra wideband (UWB) systems as the transmission signals, because those achieve the requirements inside human body, high time resolution and low transmission power and to make a smaller device [1]. Thus, we propose a method of position estimation of medical implanted devices inside the human body.

In free space, a type of position estimation algorithm is time-based technique [2], [3]. Such a technique relies on measurements of travel time of signals between nodes. So, range and position can be known because the propagation velocity of microwaves in free space is constant. On the other hand, the human body is formed of various organs with complex structures. Furthermore, each organ has different characteristics of conductivity and relative permittivity. Because, propagation velocity inside human body is expressed as a function of the relative permittivity. For this reason, medical implanted devices placed in different positions cause different propagation velocities due to the EM waves travel through different tissues or organs. Furthermore, the received signal so distorted through the multipath channel caused by the refraction at the boundary of tissues inside human body [6], [7]. As a result, position estimation errors may occur.

In this paper, we suppose the positioning of medical implanted devices in daily life that MRI and CT system don't exist around us. In this condition, a number of anchoring point is set beforehand and we estimate the position of medical implanted devices cosidering that the medical implanted devices move inside human body like the GPS system. On the premise that diagnostic images of inside human body can be obtained by magnetic resonance imaging (MRI) and computer tomography (CT) at the hospital. In analysis, we use the finite-difference time-domain (FDTD) method [5], which has been widely used to simulate the propagation of electromagnetic waves in biomedical tissues, considering the complex structure of the human body. We analyze the wave propagation inside the human body channel by FDTD method. At first, we calculate the propagation time based on the output of the correlator between the transmitter and the receiver. We apply an adaptive template synthesis method in multipath channel [4] for calculating the propagation time accurately. Furthermore, we estimate the propagation velocity inside human body. We divide the images into regions in order to estimate the relative permittivity of such regions. Then, we estimate the propagation velocity between implanted devices. Finally, we estimate the position of medical implanted devices with a time-based least squares (LS) positioning approach [6], [7].

This paper is organized as follows: In Sect. 2, position

Manuscript received May 2, 2008.
Manuscript revised August 17, 2008.

[†]The authors are with the Division of Electrical and Computer Engineering, Faculty of Engineering, Yokohama National University, Yokohama-shi, 240-8501 Japan.
a) E-mail: makoto@kohnolab.dnj.ynu.ac.jp
b) E-mail: kohno@ynu.ac.jp

DOI: 10.1587/transcom.E92.B.403

estimation using UWB signal is described. In Sect. 3, some basic characteristics of EM wave propagation and properties of dielectric materials which involve the human body tissue are described. The adaptive template synthesis method in multipath channel is described in Sect. 4. The proposed position estimation method is presented in Sect. 5. Simulation results are drawn in Sect. 6. Finally, conclusions are delineated in Sect. 7.

2. Positioning Using Ultra Wideband Signals

Locating a node in a wireless system involves the collection of location data from radio signals traveling between the target node and a number of reference nodes. Depending on the positioning technique, the angle of arrival (AOA), the signal strength (SS), or time delay information can be used to determine the location of a node. The AOA technique measures the angles between a given node and a number of reference nodes to estimate the location, while the SS and time-based approaches estimate the distance between nodes by measuring the energy and the travel time of the received signal, respectively.

Particularly, the accuracy of a time-based approach can be improved by increasing the SNR or the effective signal's bandwidth. Since UWB signals have very large bandwidth, it allows extremely accurate position estimation through time-based techniques. The main time-based techniques are the time of arrival (TOA) technique and the time difference of arrival (TDOA) technique. In the former technique, there is synchronization between a given node and the reference nodes. Whereas in the latter technique, there is synchronization among the reference nodes. An estimate of the arrival's time is obtained using a correlation receiver. In this approach the time shift of the template signal that yields the largest cross correlation with the received signal gives the desired estimate. Moreover, the TOA-based scheme estimates the location of the node using the least squares (LS) approach. The LS approach is given by

$$\hat{\theta} = min \sum_{i=1}^{N} [\tau_i - d_i(\theta)/c]^2 \tag{1}$$

where N is the number of reference nodes, τ_i is the i^{th} TOA measurement, $d_i(\theta) = \|\theta - \theta_i\|$ is the distance between the given node and the ith reference node, with θ and θ_i denoting their locations, respectively [2], [3].

In this paper, we adopt the time-based LS approach which can take advantage of the characteristic of UWB systems which achieve high time resolution.

3. Radio Propagation in a Medium

3.1 Electric Constant of Human Body Tissues

A human body consists of various organs with complex structures. Furthermore, each organ has different characteristics of the electrical constants which are conductivity and permittivity.

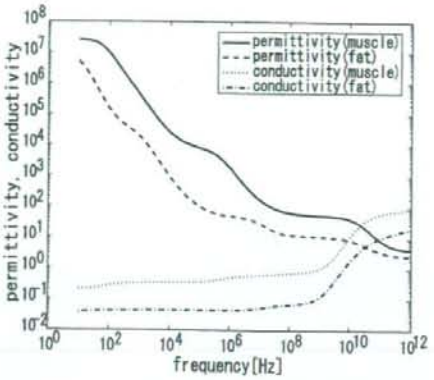

Fig. 1 Dielectric parameters of muscle and fat.

We should consider the frequency band when we try to estimate the position of implanted devices using UWB radios. Indeed, the electromagnetic wave propagation in dispersive biological tissues is frequency dependent on permittivity and conductivity. The Cole-Cole model [6], [7]. describes the frequency dependency of the complex permittivity. Figure 1 shows the relative permittivity and conductivity of muscle and fat.

Furthermore, the propagation velocity of a homogeneous tissue is given by

$$v(\omega) = \frac{c}{\sqrt{\varepsilon_r(\omega)}} \tag{2}$$

where c is the velocity of light in the free space and $\varepsilon_r(\omega)$ is the relative permittivity of a human tissue. So propagation velocity has frequency dependency and differs by different body tissues. Because of this, a pulse broadening of a received UWB signal is caused by the group delay. Furthermore, the received signal so distorted through the multipath channel caused by the refraction at the boundary of tissues and the channel of frequency dependency inside human body.

4. Adaptive Template Synthesis Method in Multipath Channel

As mentioned above, the received signal so distorted and pulse broadening through the human body channel. When we calculate the propagation time based on the output of the correlator between the transmitter and the receiver, we need to use the template signal considering the received signal distorted and pulse broadening. So we use the adaptive template synthesis method for UWB receiver to calculate the propagation time based on the output of the correlator accurately [4].

The template waveform is constructed as combination of orthogonalized elementary waveforms with certain coefficients. Generally, every UWB signal can be decomposed into some orthgonal elementary waveforms such as sine

waves by Fourier series expansion independent of its kernel function. It is therefore possible to approximately construct a UWB template waveform by expanding the UWB signal into the weighted sum of several orthogonal elementary waveforms and truncating it to finite order. The synthesized template waveform is described as

$$w(t) = \sum_{k=1}^{N} C_k \int_{-\frac{T}{2}}^{\frac{T}{2}} L_k(t) \times W_{env}(t) dt \tag{3}$$

where $L_k(t)$ are the orthogonal elementary waveform and C_k are the Corresponding coefficient. $W_{env}(t)$ is the envelope which truncates each elementary waveform to finite duration. Rectangular window is used as $W_{env}(t)$, that is

$$W_{env}(t) = \begin{cases} 1 & \left(|t| \le \dfrac{T}{2}\right) \\ 0 & (others) \end{cases} \tag{4}$$

Generally, the coefficients C_k are derived as follows

$$C_k = \frac{2}{T} \int_{-\frac{T}{2}}^{\frac{T}{2}} r_s(t) L_k(t) dt \tag{5}$$

where T is the pulse duration. If the set of orthogonal elementary waveform $L_k(t)$ is complete, the synthesized template strictly matches to the ideal one. In reality, however, the number of coefficient and elementary waveforms should be finite. The coefficient vector $\mathbf{C}$ whose element is described as Eq. (5) is truncated to finite order.

In multipath channel such as the human body channel with very close range communication, we mainly consider Intra-pulse Interference (IPI) problem which is occurred when the multipath components are distributed more closely than typical pulse width. We use trigonometric function as orthogonal basis because it is closely-related to frequency domain and there is a possibility that we may analyze the human body channel in frequency domain.

We set $\mathbf{w}$ to be unit energy for normalization purposes and it is written in vector representation as follows,

$$\mathbf{w} = \sum_{j=1}^{N} C_j \mathbf{L}_j \tag{6}$$

The above equation is equivalent to Eq. (3). $\mathbf{w}$ is vector based description of template waveform $w(t)$, whose size is $(n \times 1)$. $\mathbf{L}_j$ denotes the orthonormal basis used to synthesize the template waveform and it is also written in vector form as follows,

$$\mathbf{L}_j = [L_{j1} \; L_{j2} \; \cdots \; L_{jn}]^t \quad (for \; j = 1, 2, \cdots, N) \tag{7}$$

where N is the number of orthonormal basis used for synthesis and each orthonormal basis consists of n samples. Here, we set an $(n \times N)$ matrix $\mathbf{M}$ whose jth column is $\mathbf{L}_j$, that is

$$\mathbf{M} = [\mathbf{L}_1 \; \mathbf{L}_2 \; \cdots \; \mathbf{L}_N] \tag{8}$$

In this case, w in Eq. (6) reduces to

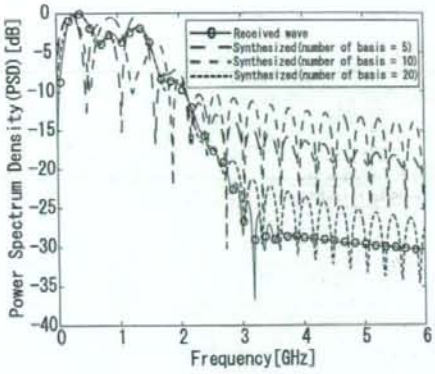

Fig. 2 Spectrum of synthesized template waveform and one of the received wave inside human body channel.

$$\mathbf{w} = \mathbf{M} \cdot \mathbf{C}^t \tag{9}$$

We also set an $(n \times P)$ matrix $\mathbf{A}$ whose kth column is $\mathbf{r}_k$, that is

$$\mathbf{A} = [\mathbf{r}_1 \; \mathbf{r}_2 \; \cdots \; \mathbf{r}_P] \tag{10}$$

where P is the number of pilot symbols. From Eq. (9) and Eq. (10), it can be derived that $\mathbf{w}^t \cdot \mathbf{A}$ forms $(1 \times P)$ vector, whose kth element is $< \mathbf{r}_k, \mathbf{w} >$. Therefore

$$\begin{aligned} F &= \sum_{k=1}^{P} |\langle \mathbf{r}_k, \mathbf{w} \rangle|^2 \\ &= (\mathbf{w}^t \cdot \mathbf{A}) \cdot (\mathbf{w}^t \cdot \mathbf{A})^t \\ &= (\mathbf{C} \cdot \mathbf{M}^t \cdot \mathbf{A}) \cdot (\mathbf{A}^t \cdot \mathbf{M} \cdot \mathbf{C}^t) \end{aligned} \tag{11}$$

Eq. (11) can be transformed as

$$F = \mathbf{C} \cdot (\lambda \cdot \mathbf{C}^t) = \lambda \cdot \|\mathbf{C}\|^2 \tag{12}$$

where λ is eigen value of $(N \times N)$ square matrix $(\mathbf{M}^t \cdot \mathbf{A}) \cdot (\mathbf{A}^t \cdot \mathbf{M})$. In order to make the function F maximum, the eigen value in Eq. (12) should be maximum. Therefore the optimal coefficient vector $\mathbf{C}$ is supposed to be simply the normalized eigen vector of matrix $(\mathbf{M}^t \cdot \mathbf{A}) \cdot (\mathbf{A}^t \cdot \mathbf{M})$ corresponding to its largest eigen value. By using P pilot symbols included in each packet, the coefficient vector $\mathbf{C}$ is derived adaptively as shown in Eq. (11) and Eq. (12). The template waveform can be synthesized using this coefficient vector C as described in Eq. (9).

Figure 2 shows spectrum of synthesized template waveform and one of the received wave inside human body channel. It can be seen form Fig. 2 that synthsized template waveform can well approximate the one of the received wave through the human body channel.

5. Proposed Method of Position Estimation

5.1 Relative Permittivity of Homogeneous Tissue

Although relative permittivity of a human body tissue is fre-

Table 1 Calculation parameters of FDTD analysis.

Analysis Model	Body Model of Remcom Co., Ltd.
Transmit Waveform	Gaussian Mono Pulse
Used Band Frequency	0 ~ 4.0 [GHz]
Time Step	1.926 [ps]
spacial step	Δ x = 1 [mm], Δ y = 1 [mm]
lattice size	1 [mm] × 1 [mm]
grid configuration	square
boundary conditions	Perfect Electrical Conductor(PEC)

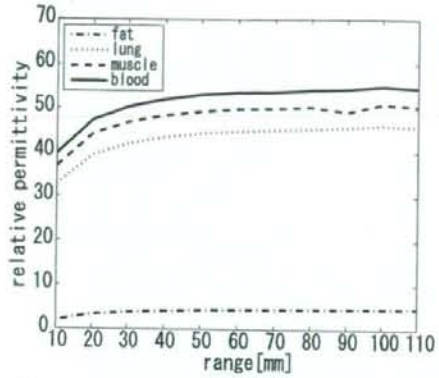

Fig. 3 Distance property of relative permittivity of human homogeneous tissues.

Table 2 The average relative permittivity of human body tissues.

Tissue	muscle	fat	blood	intestine
ε_r	47.83	4.08	51.59	50.67
Tissue	stomach	tendon	bone	bladder
ε_r	56.99	37.61	17.09	64.63

quency dependent, in this paper, the arrival's time is obtained by using a correlation receiver. So, the relative permittivity can be rewritten as

$$\varepsilon_r = \left(\frac{c\,t_a}{d}\right)^2 \tag{13}$$

where t_a is the arrival's time based on the output of the correlator with adaptive template wave considering the received signal distorted and pulse broadening, and d is the propagation distance in a homogeneous tissue.

We analyze the relative permittivity of human homogeneous tissues using the FDTD method [5]. The calculation parameters of FDTD analysis are are listed in Table 1. Figure 3 shows the relative permittivity in function of the distance d. We take the average relative permittivity of eight tissues, which are listed in Table 2.

5.2 Proposed Method of Position Estimation

We proposed a position estimation method by estimating the propagation velocity inside of a human body. In addition to it, we calculate the propagation time from arbitrary tag points to node points (whose position is known) by using the

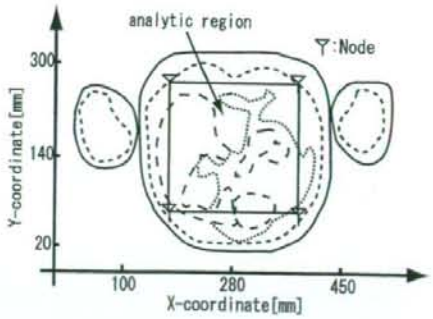

Fig. 4 System model of the first stage.

estimated propagation velocity. Finally, we estimate the position of medical implanted devices using the LS approach.

The applicable conditions of this method are next two conditions. The first is that the two-dimensional images inside human body are obtained and we can know the tissue distribution inside human body. Furthermore, the second is that the value of relative permittivity of each human body tissue is obtained.

The images of inside of the human body are acquired beforehand from a MRI or CT system. Our proposed method uses four medical implanted devices, whose locations are known, and we call them "node" in this paper. On the other hand, there is a medical implanted device, whose location is unknown, and we call it "tag" in this paper.

Our proposed method is composed of two stages. It is very difficult to estimate the real propagation velocity from all arbitrary tag points to node point directly. So, the real propagation velocity is estimated by the images of inside human body obtained from MRI or CT systems beforehand. So, we have large volumes of data of the real propagation velocity. Hence, we estimate the propagation velocity with two stages to simplify the estimation and to reduce the amount of data.

5.2.1 First Stage

The procedure of the first stage is as follows. Figure 4 shows the system model of the first stage. At first, we calculate the average relative permittivity of the region delimited by four nodes. The average relative permittivity ε_{ave} and propagation velocity v_{ave} are calculated as

$$\varepsilon_{ave} = \sum_{i=1}^{I} (\varepsilon_{r(i)}\, p_{r(i)}) \tag{14}$$

$$v_{ave} = \frac{c}{\sqrt{\varepsilon_{ave}}} \tag{15}$$

where n is node number, I total number of tissues, $\varepsilon_{r(i)}$ is the ε_r of a homogeneous tissue listed in Table 1, and $p_{r(i)}$ is a percentage of the i^{th} tissue [8].

Secondly, we calculate the propagation time $t^1_{n(x,y)}$ from four nodes to an arbitrary point in the studied region using

v_{ave}. The propagation time in the first stage for the n^{th} node $t^1_{n(x,y)}$ is calculated as

$$t^1_{n(x,y)} = \frac{d_{n(x,y)}}{v_{ave}} \tag{16}$$

where x is x-coordinate of an arbitrary point, y is y-coordinate of an arbitrary point, $d_{n(x,y)}$ is a direct length of a path from an arbitrary point to the four nodes, respectively. Also, x, y have 1 mm of separation.

Then, we estimate the travel times t_n of the received signal from the tag point to the four nodes by using a correlation receiver. In this approach, the desired estimation is given by the time shift of the template signal that yields the largest cross correlation with the received signal.

Finally, we estimate the position of tag using the LS approach.

$$\theta(x,y)_1 = min \sum_{n=1}^{4} [t_n - t^1_{n(x,y)}]^2 \tag{17}$$

where $\theta(x,y)_1$ is the estimate position of the first stage.

5.2.2 Second Stage

In the stage, we use $\theta(x,y)_1$, which is obtained from Eq.(17).

Firstly, we divide the images inside of the human body into several regions and estimate relative permittivity of a respective region. Figure 5 shows the system model of the second stage with (3 × 3) regions. A relative permittivity of one region is calculated as

$$\varepsilon_j = \sum_{i=1}^{I} (\varepsilon_{r(i)}\, p_{r(i)}) \tag{18}$$

where j is a region number, i is a tissue number, ε_j is an average relative permittivity of j^{th} region, $\varepsilon_{r(i)}$ is the ε_r of a homogeneous tissue listed in Table 1, and $p_{r(i)}$ is a percentage of the i^{th} tissue in the j^{th} region.

Secondly, we estimate the relative permittivity ε_n and propagation velocity v_n of the paths from four nodes to $\theta(x,y)_1$.

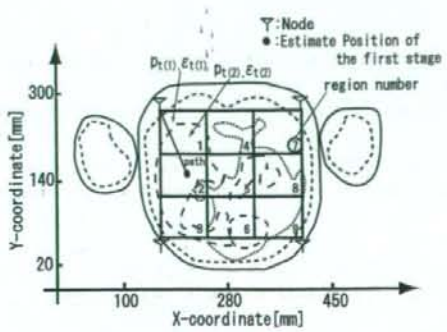

Fig. 5 (3 × 3) regions system model of the second stage.

$$\varepsilon_n = \frac{\sum_{k=1}^{K} (\varepsilon_k\, d_k)}{d_{all}} \tag{19}$$

$$v_n = \frac{c}{\sqrt{\varepsilon_n}} \tag{20}$$

where K is a number of regions through the propagation path from the n^{th} node to $\theta(x,y)_1$, d_k is a length of the path through the k^{th} region, and d_{all} is a direct length of the path from n^{th} node to $\theta(x,y)_1$.

Then, we calculate the propagation time $t^2_{n(x,y)}$ from four nodes to an arbitrary point using v_n. The propagation time $t^2_{n(x,y)}$ is calculated as

$$t^2_{n(x,y)} = \frac{d_{n(x,y)}}{v_n} \tag{21}$$

where x is x-coordinate of an arbitrary point, y is y-coordinate of an arbitrary point, and $d_{n(x,y)}$ is a length of a path from an arbitrary point to four nodes, respectively. And x, y have 1 mm of separation.

Finally, we estimate the position of tag using the LS approach.

$$\theta(x,y)_2 = min \sum_{n=1}^{4} [t_n - t^2_{n(x,y)}]^2 \tag{22}$$

where t_n is the travel time of the received signal from tag to the four nodes, and $\theta(x,y)_2$ is the estimate position of the second stage.

6. Numerical Simulation

This section presents simulations to demonstrate the performance of the proposed method.

6.1 Simulation Model

The images of MRI or CT system are two-dimensional images. In this paper, we consider only two-dimensional images. Figure 6 shows the simulation image obtained by the FDTD of Remcom Co., Ltd. In addition, Fig. 7 shows a simplified image of Fig. 6. This two-dimensional image is a cross-section of a human body at high 137.5 cm. This model contains human body tissues such as muscle, fat, blood, bone, stomach, intestine, bladder, tendon. As mentioned before, we consider four nodes at positions (171, 61), (400, 61), (171, 240), and (400, 240). On the other hand, there is one tag device. Furthermore, we premise the omnidirectional dipole antenna in this study. However, we simulate with the channel model containing both a channel characteristic inside human body and transmitting and receiving antenna characteristics. So specific antenna structure and characteristic are not considered in this simulation.

6.2 Bandwidth of UWB Signal and Accuracy of Position Estimation

Before we simulate the proposed method, we analyze the

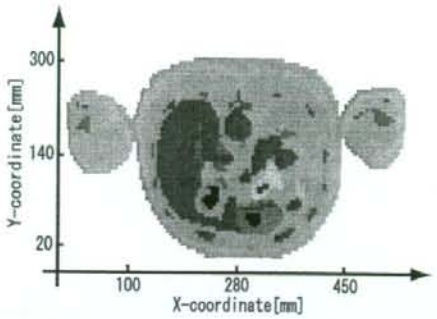

Fig. 6 Sliced 2D human body image of position of 137.5 cm high of human body model of Remcom Co., Ltd.

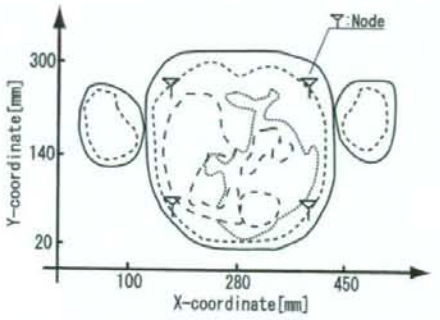

Fig. 7 Simplified 2D human body model of position of 137.5 cm high.

bandwidth of UWB signals and the accuracy of position estimation. Generally, as bandwidth of UWB signal becomes larger, ranging and position estimation accuracy are better, because a large bandwidth of UWB signal provides a high-resolution time. However, inside human body, the high-frequency components are attenuated. So, there is a limit in the accuracy of position estimation. We simulate a position estimation accuracy for several bandwidths of UWB signals. Figure 8 shows the simulation result. The horizontal axis shows a bandwidth of a UWB pulse and the vertical axis shows the RMSE of position estimation. In the Fig. 8, position estimation accuracy is better from 1 GHz bandwidth to 4 GHz bandwidth. However, over 4 GHz bandwidth, the position estimation accuracy remains the same, because received pulse is distorted by the attenuation of high-frequency components. Based on this result, we use UWB signals of 4 GHz bandwidth.

6.3 Performance Evaluation of Our Proposed Method

We evaluate the performance of our proposed method. In this paper, we consider the human body channel as the static model. At the second stage, we divide the large region inside of the four nodes into some smaller regions. The number of partitions is (3 × 3), (5 × 5), and (7 × 7) for x-direction and y-direction. We compare the proposal with the method using the average relative permittivity obtained in Table 1, in

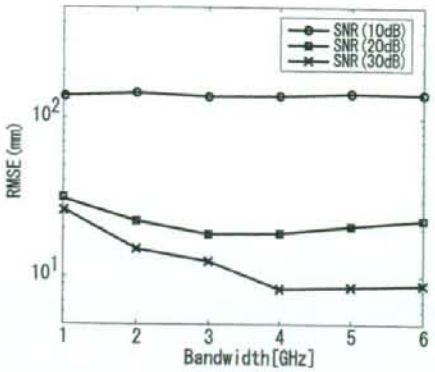

Fig. 8 Relation between RMSE and bandwidth of UWB signal.

Table 3 Simulation specification.

Analysis Model	Body Model of Remcom Co., Ltd.
Transmit Waveform	Gaussian Mono Pulse
Used Band Frequency	0 ~ 4.0 [GHz]
Time Step	1.926 [ps]
Sequence	MLS(length=7)
Pulse Interval	5000 [time steps]
Number of Time Step	40000
Kind of Noise	AWGN

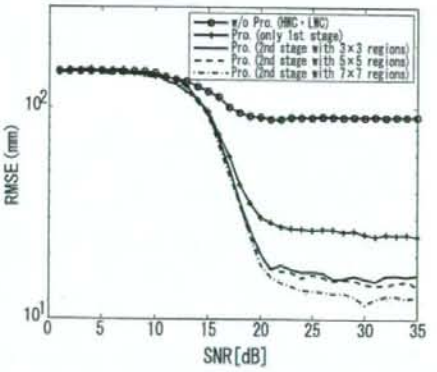

Fig. 9 Comparison of positioning error of the 1st stage and the 2nd stage of our proposed method.

order to estimate the propagation velocity from all arbitrary tag points to a node point. The average relative permittivity inside the human body is assumed to be 2/3 of muscle and 1/3 of fat. The proportion of the tissue of high water content (HWC) to the low water content (LWC) is 2:1 in a human body, where the typical tissue of HWC is muscle and fat for LWC. The simulation specifications are listed in Table 3.

Figure 9 shows the result of position estimation. The horizontal axis shows SNR and the vertical axis shows RMSE of position estimation. Simulation results show that accuracy of proposed method of positioning is around the size of medical implanted device such as a capsule endoscopes. In addition, simulation results show that when the